Article:
Takemura, T. and Healy, D. (2026) Anisotropic stress-induced permeability change in cracked rock during the crack closure stage: A tensorial approach incorporating tortuosity and bottlenecks. Tectonophysics, 927. 231127. ISSN: 0040-1951

https://doi.org/10.1016/j.tecto.2026.231127

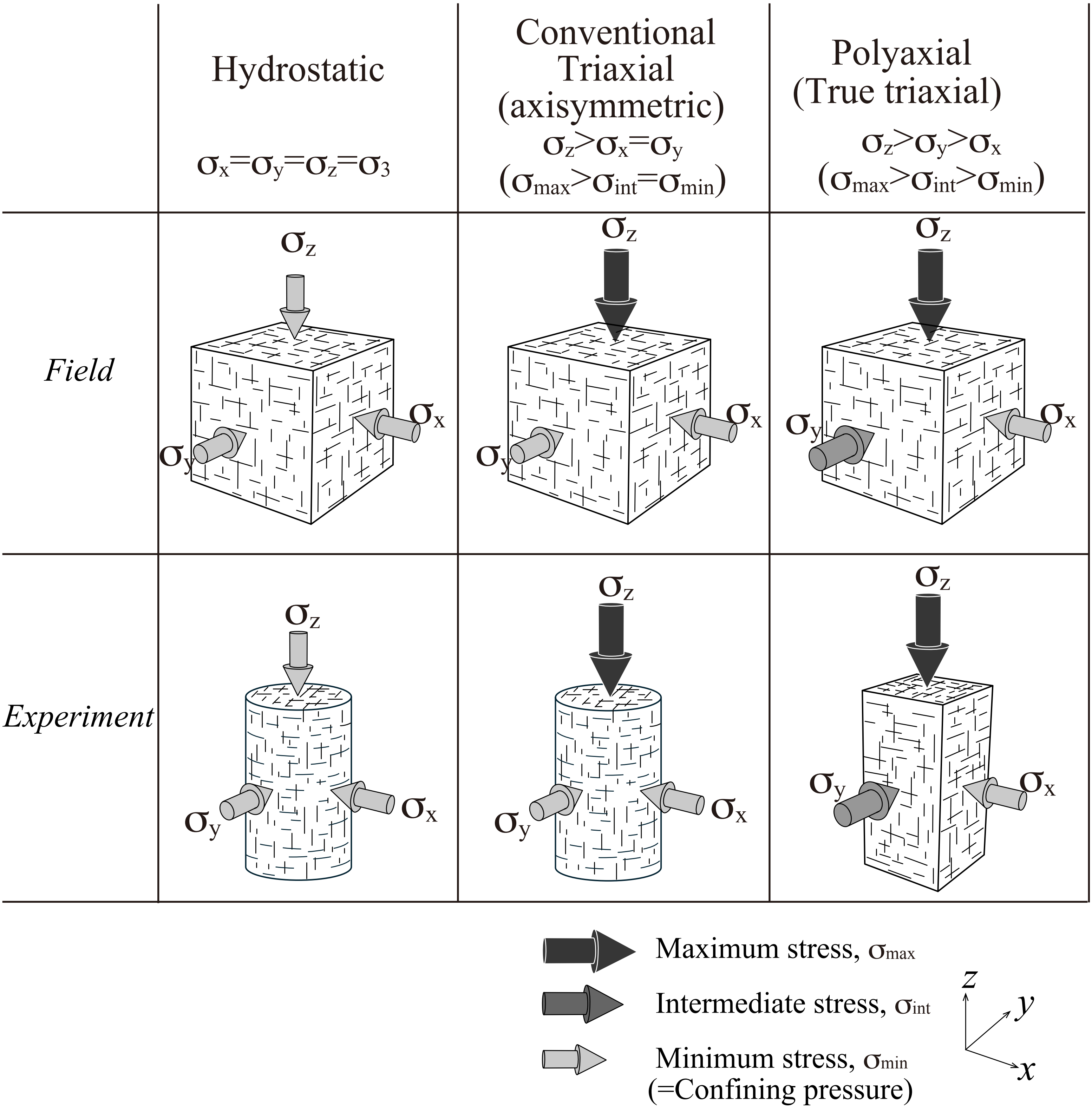

Fig. 1

Fig. 1. Schematic illustration of the three types of stress conditions applied to the rock in this study.

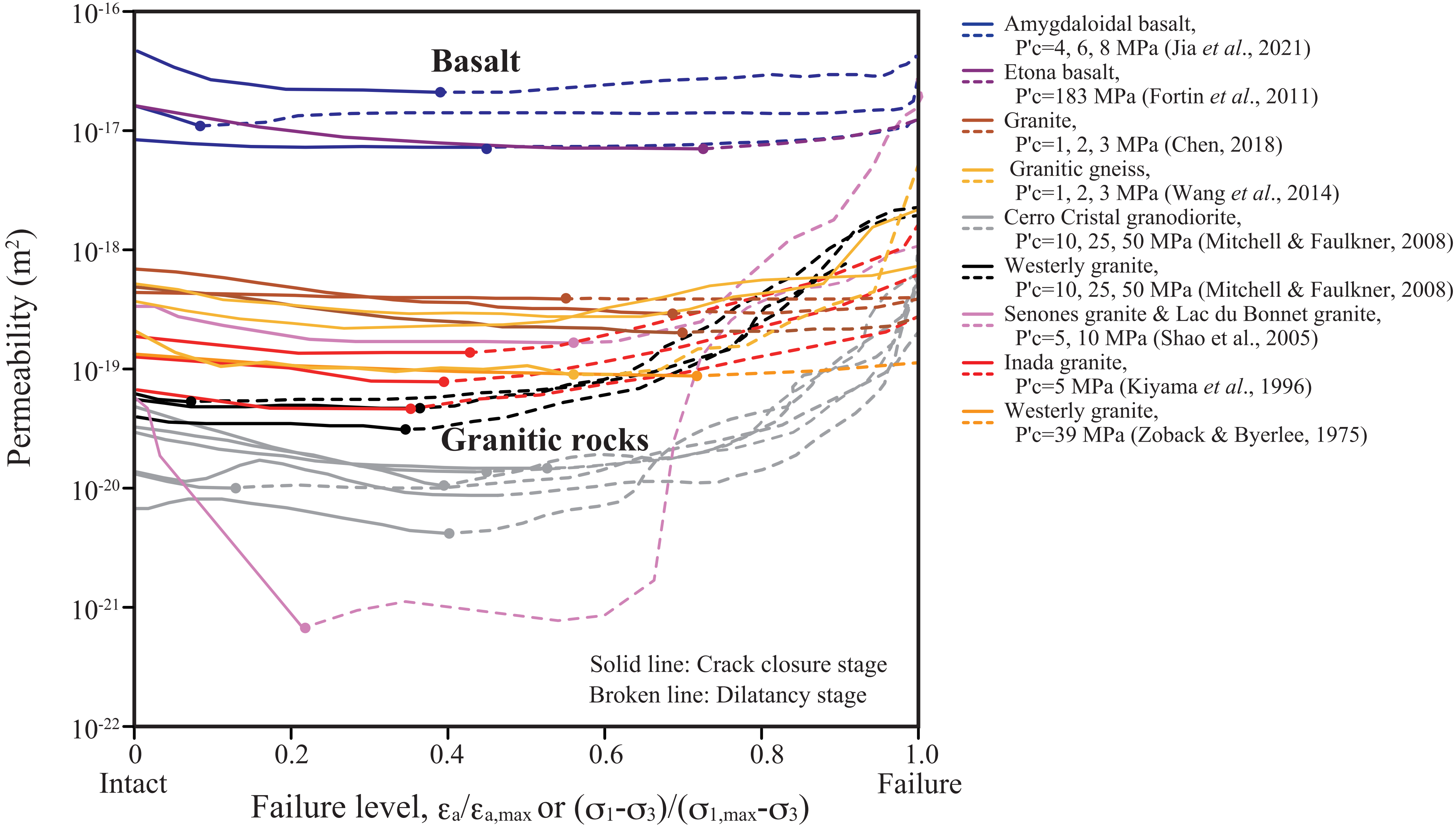

Fig. 2

Fig. 2. Change in permeability with increasing differential stress up to the failure stress under conventional triaxial testing of basalt (Fortin et al., 2011; Jia et al., 2021) and granitic rocks (Chen, 2018; Kiyama et al., 1996; Mitchell and Faulkner, 2008; Shao et al., 2005; Wang et al., 2014; Zoback and Byerlee, 1975). The abscissa represents the dimensionless failure level calculated from the axial strain, ε_a, or differential stress, σ_1-σ_3 as reported in the respective studies. Here, the subscript 'max' denotes the value at failure, and the solid and broken lines correspond to the crack closure and dilatancy stages, respectively. In the legend, P'_C denotes the effective confining pressure.

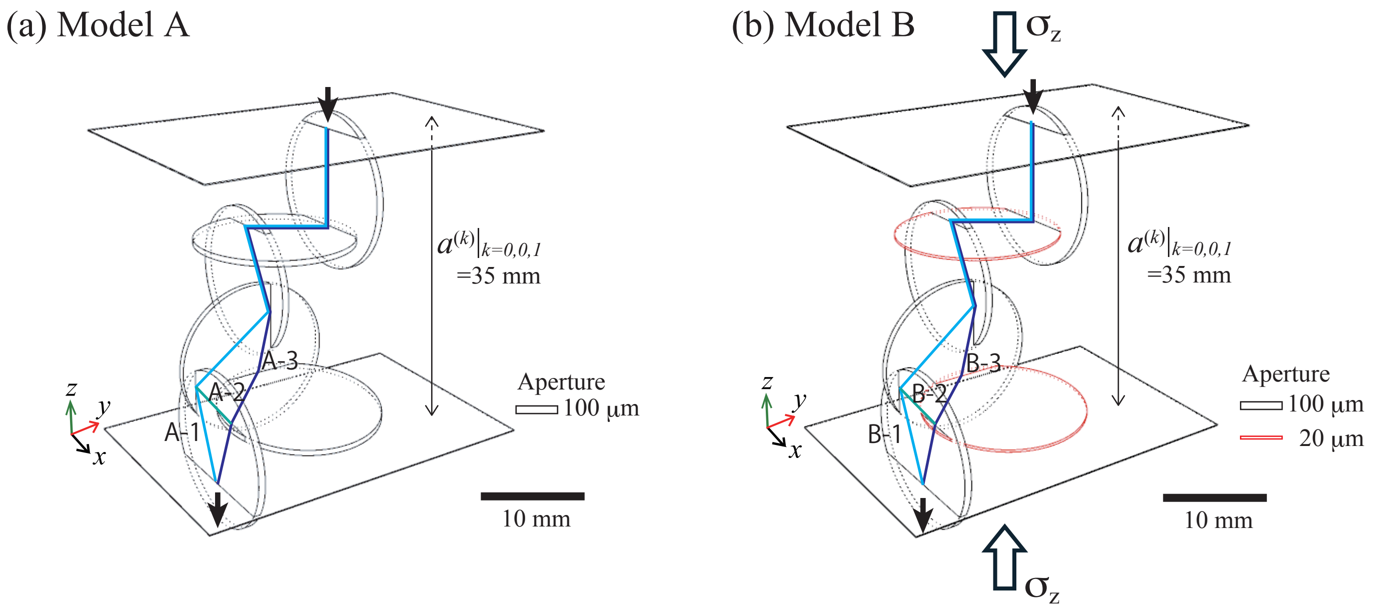

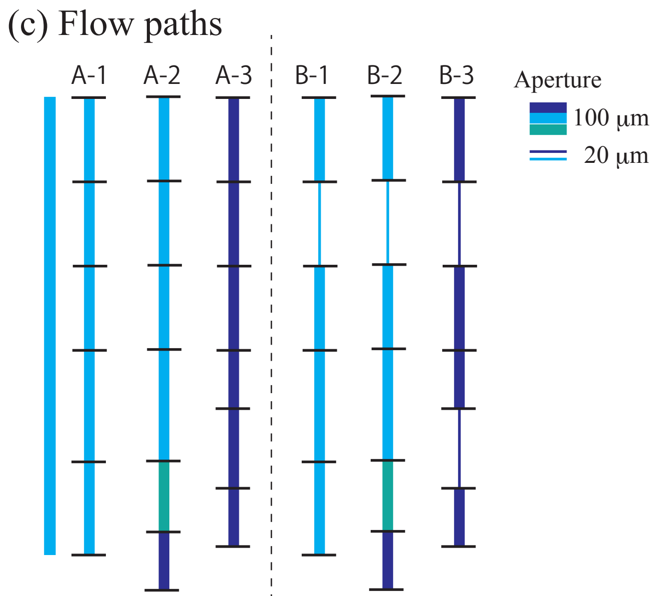

(d) Summary of Parameters

	A-1	A-2	A-3	B-1	B-2	B-3
$\tau^{(k)}\|_{k=0,0,1}$	1.58	1.70	1.54	1.56	1.68	1.54
$\bar{L}^{(k)}$	54.3	58.6	53.4	54.3	58.6	53.4
Aperture-weighted path length $\bar{L}^{(k)}/t$	543	586	534	943	986	1294
$\beta^{(k)}\|_{k=0,0,1}$	1.00	1.00	1.00	0.24	0.23	0.28
$T_{ij}\|_{i=j=3}$	1.00	1.00	1.00	1.00	1.00	1.00

Fig. 3

Fig. 3 Schematic view of the conceptual model illustrating tortuosity and bottleneck in a crack model. The crack model comprises five cracks in total: two normal to the *z*-axis, two normal to the *y*-axis, and one normal to the *x*-axis. The crack model comprises five cracks in total: two normal to the *z*-axis, two normal to the *y*-axis, and one normal to the *x*-axis. (A) the model under hydrostatic conditions and (B) the model under anisotropic stress with σ_z (red cracks oriented normal to the *z*-axis are closed by σ_z, and their aperture decreases from 100 μm to 20 μm). The fluid is assumed to flow in through the cracks at the upper end and be discharged from the cracks at the lower end, with each model having three possible flow paths. (C) Diagram of individual flow paths with aperture, and (D) shows the calculated parameters for each flow path.

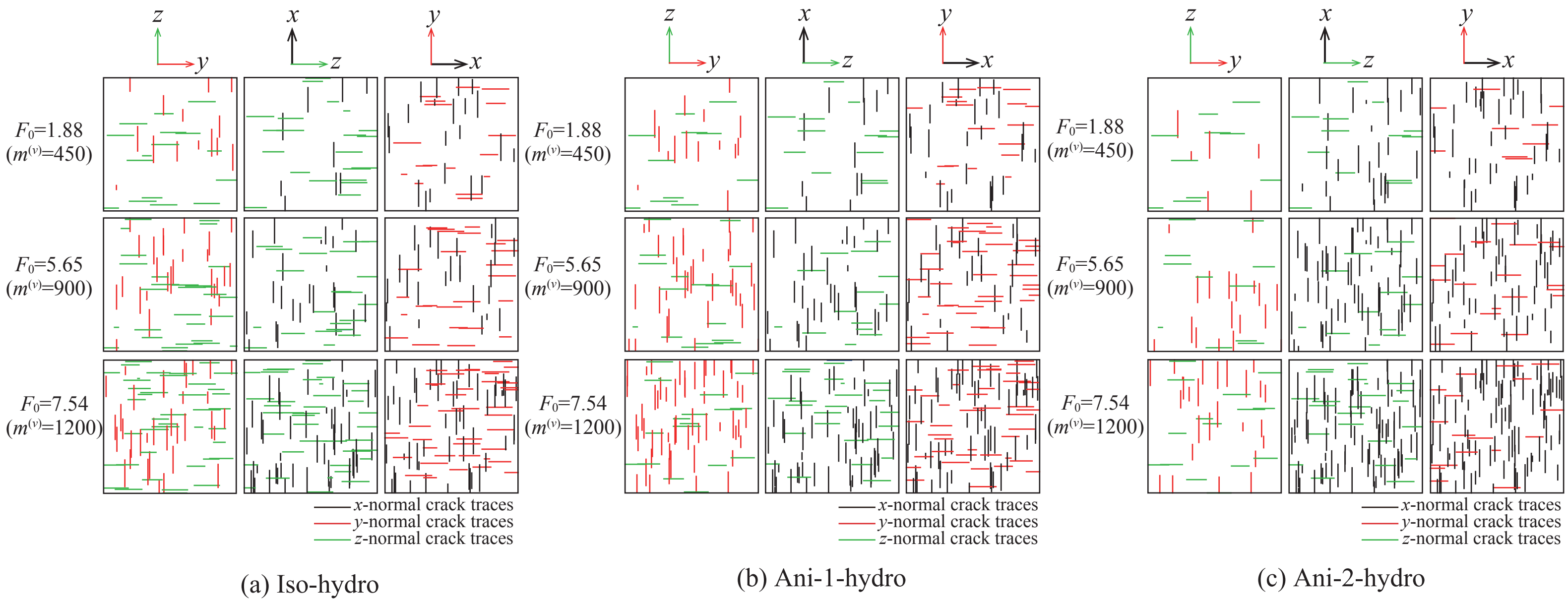

Fig. 4

Fig. 4 Crack traces observed on the *x*-, *y*-, and *z*-cross-sections for each model. The crack generation conditions are (a) isotropic (Iso), (b) weakly anisotropic (Ani-1), and (c) strongly anisotropic (Ani-2), and stress condition set as hydrostatic stress. For comparison, three different crack densities (F_0=1.88, 5.65, 7.54) are presented for each model. In the figure, the black, red, and green crack traces represent cracks with normal vectors in the *x*-, *y*-, and *z*-directions, respectively. Here, the crack generation configuration uses the instance with seed=0.

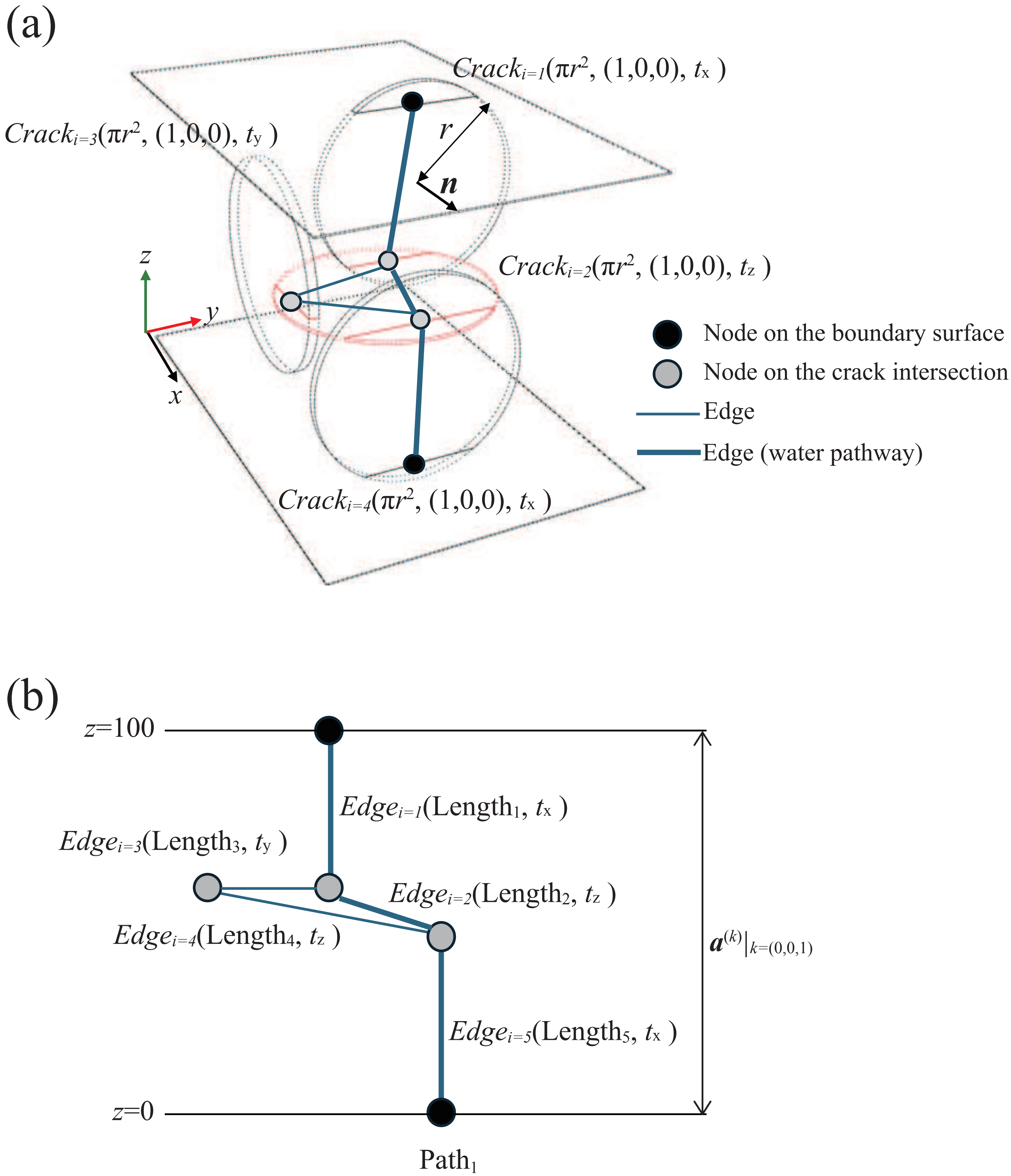

Fig. 5

Fig. 5 Conceptual schematic of the algorithm for determining tortuosity and bottlenecks numerically. The aperture of cracks not subjected to normal stress are denoted by t_x and t_y, and the red crack is subjected to normal stress with its aperture denoted by t_z. (a) Crack arrangement and percolating flow pathways in three dimensions, (b) Diagram showing only the percolating flow pathways.

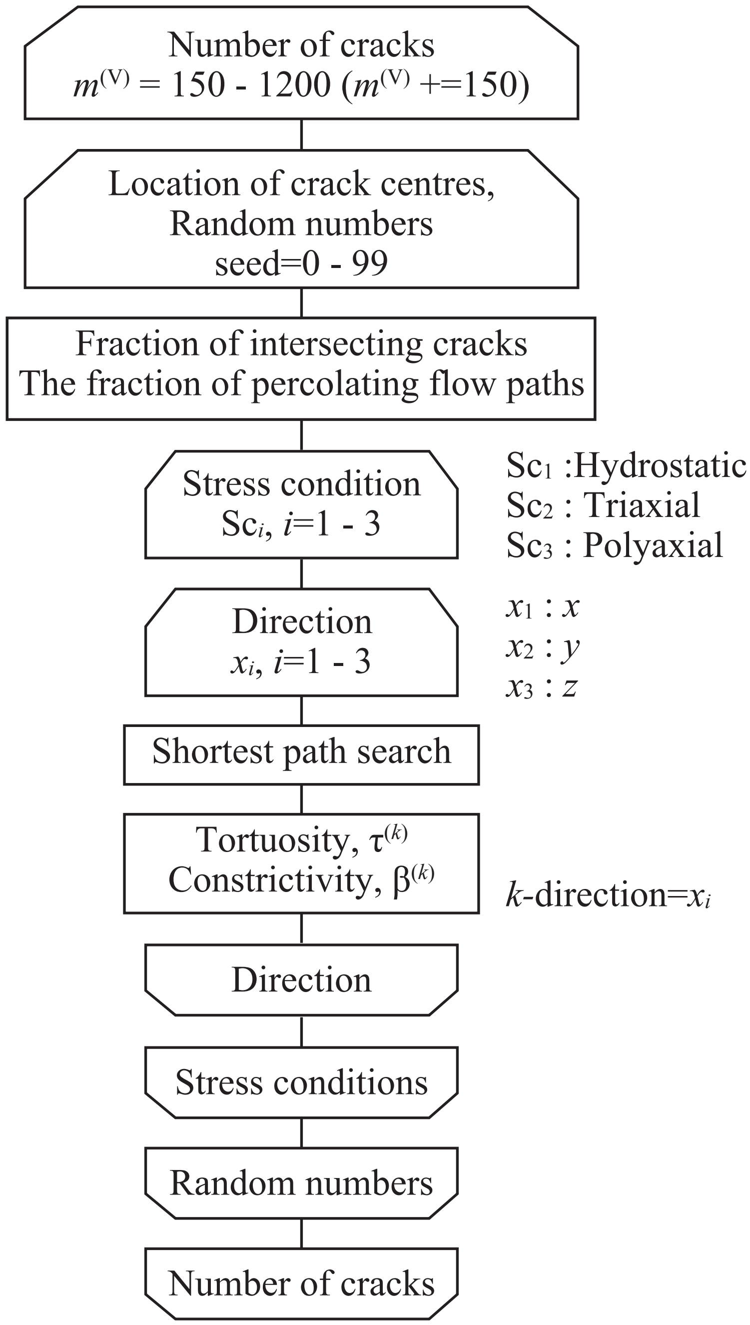

Fig. 6

Fig. 6 Flowchart illustrating the generation of the crack model and the output of parameters in this study.

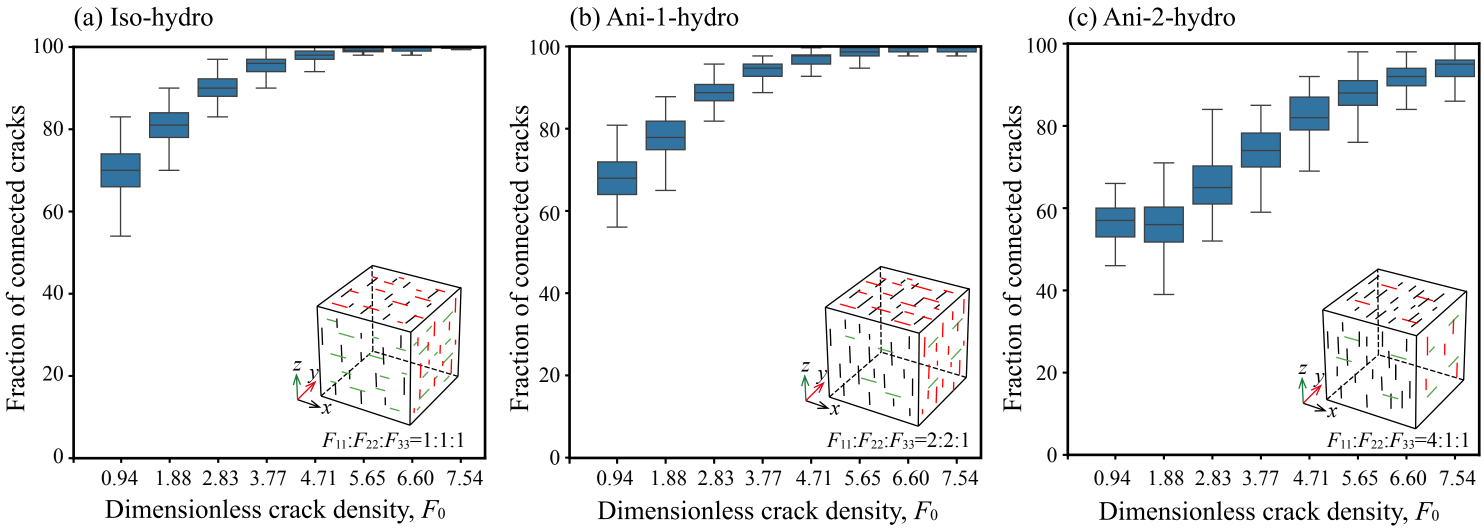

Fig. 7

Fig. 7 A box-and-whisker plot of the fraction of intersecting cracks for each crack density. Here, 100 instances are generated for each dimensionless crack density. Cracks that do not intersect become isolated cracks. Since the stress state does not influence crack intersections, results under hydrostatic conditions are shown.

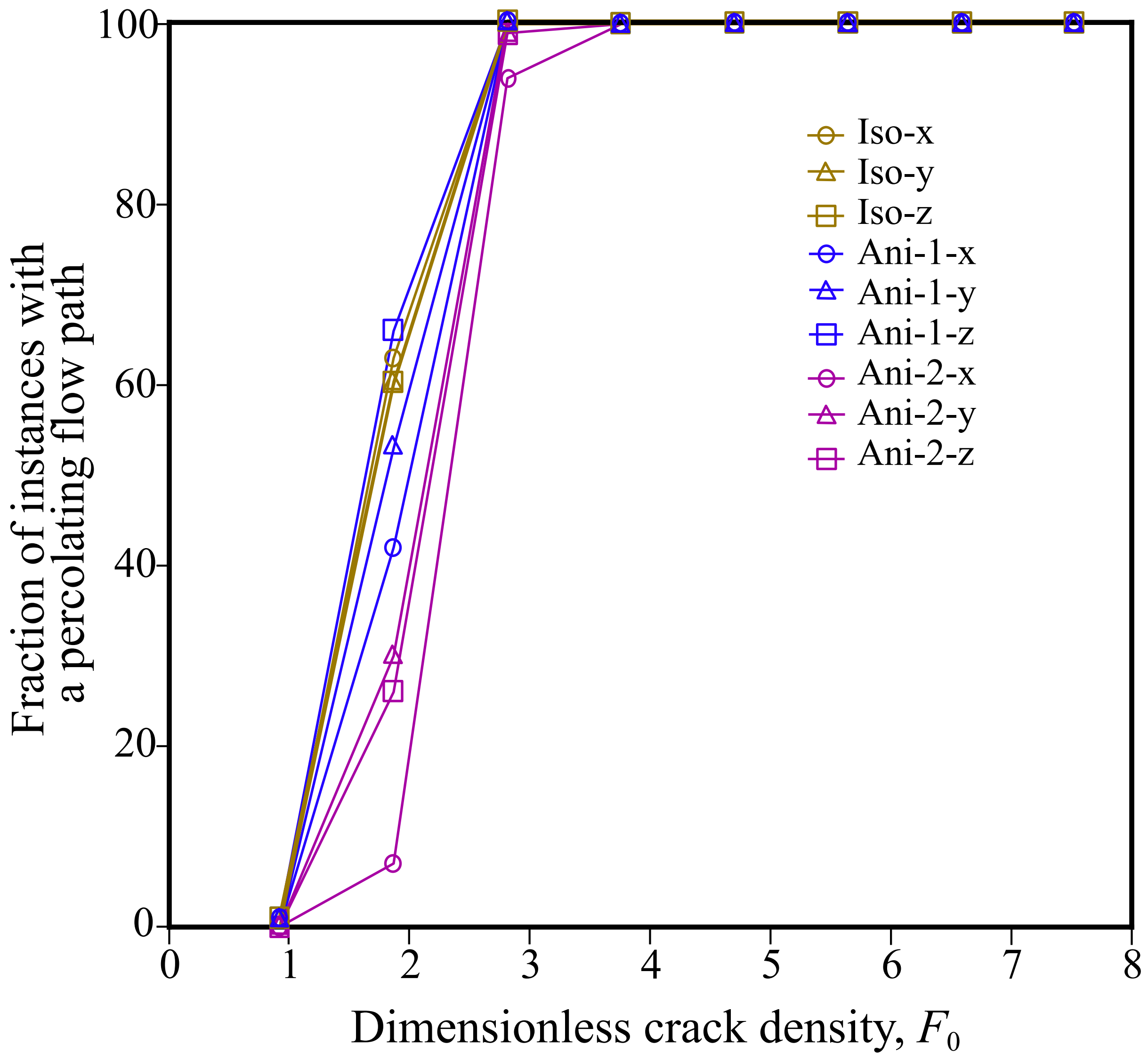

Fig. 8

Fig. 8 The fraction of instances in which a percolating flow path connecting the boundary surfaces in the *x*, *y*, and *z* directions appeared, for each crack model (Iso, Ani-1, Ani-2). Each model includes 100 randomly generated instances.

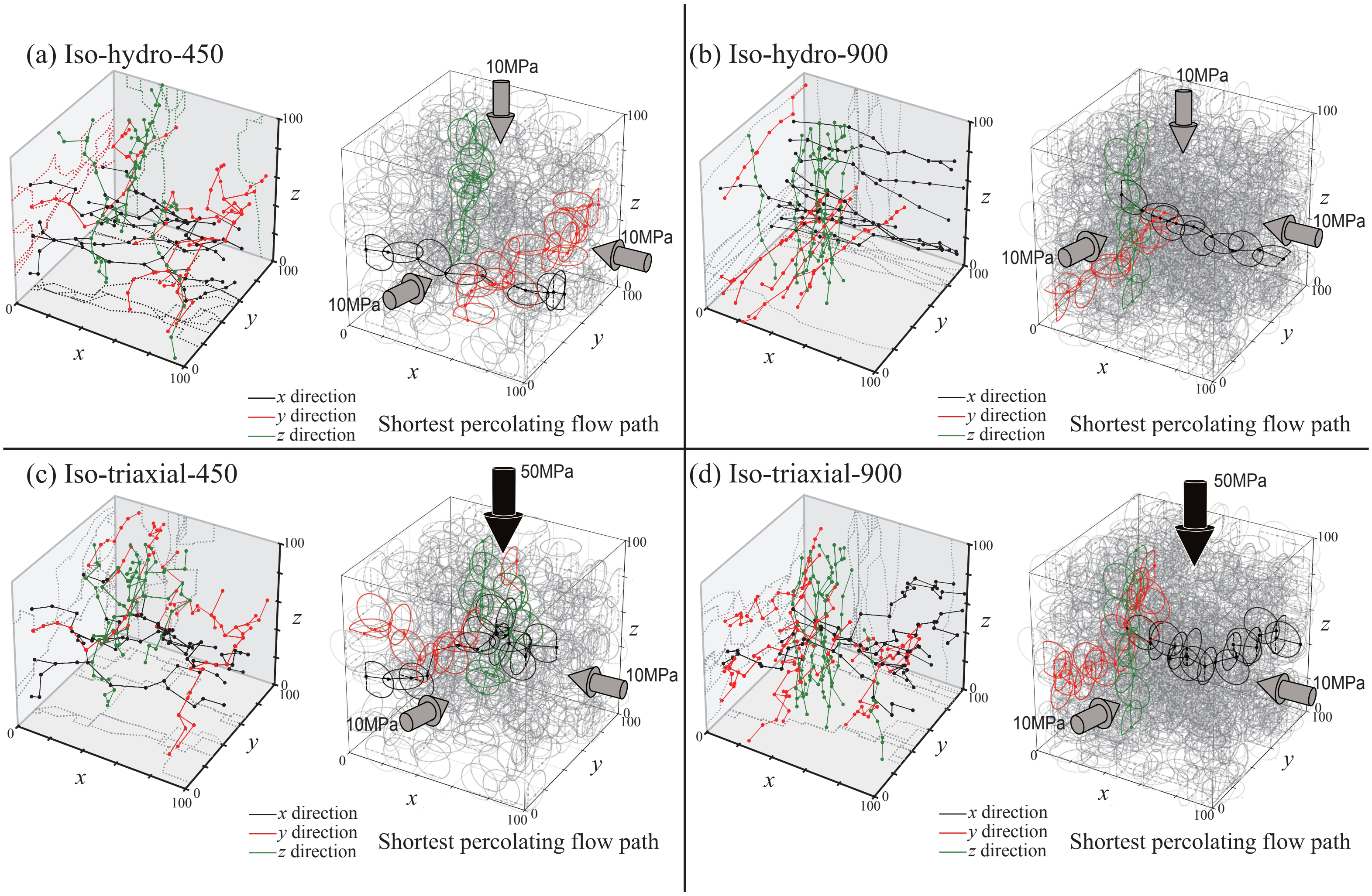

Fig. 9

Fig. 9 3D visualisations of percolating flow paths corresponding to illustrative crack densities under hydrostatic and triaxial stress conditions in an isotropically distributed crack model (Iso). Specifically: (a) crack density F_0=2.83 under hydrostatic condition (σ_x=σ_y=σ_z=10MPa), (b) crack density F_0=5.65 under hydrostatic condition (σ_x=σ_y=σ_z=10MPa), (c) crack density F_0=2.83 under triaxial condition (σ_x=σ_y=10MPa, σ_z=50MPa) and (d) crack density F_0=5.65 under triaxial condition (σ_x=σ_y=10MPa, σ_z=50MPa). Here, the crack generation condition was set using seed = 12. The points in the graph represent nodes, and the dashed lines represent their projections onto specific planes: x-direction paths are projected onto the *z*=0 plane, *y*-direction paths onto the *x*=0 plane, and *z*-direction paths onto the *y*=100 plane.

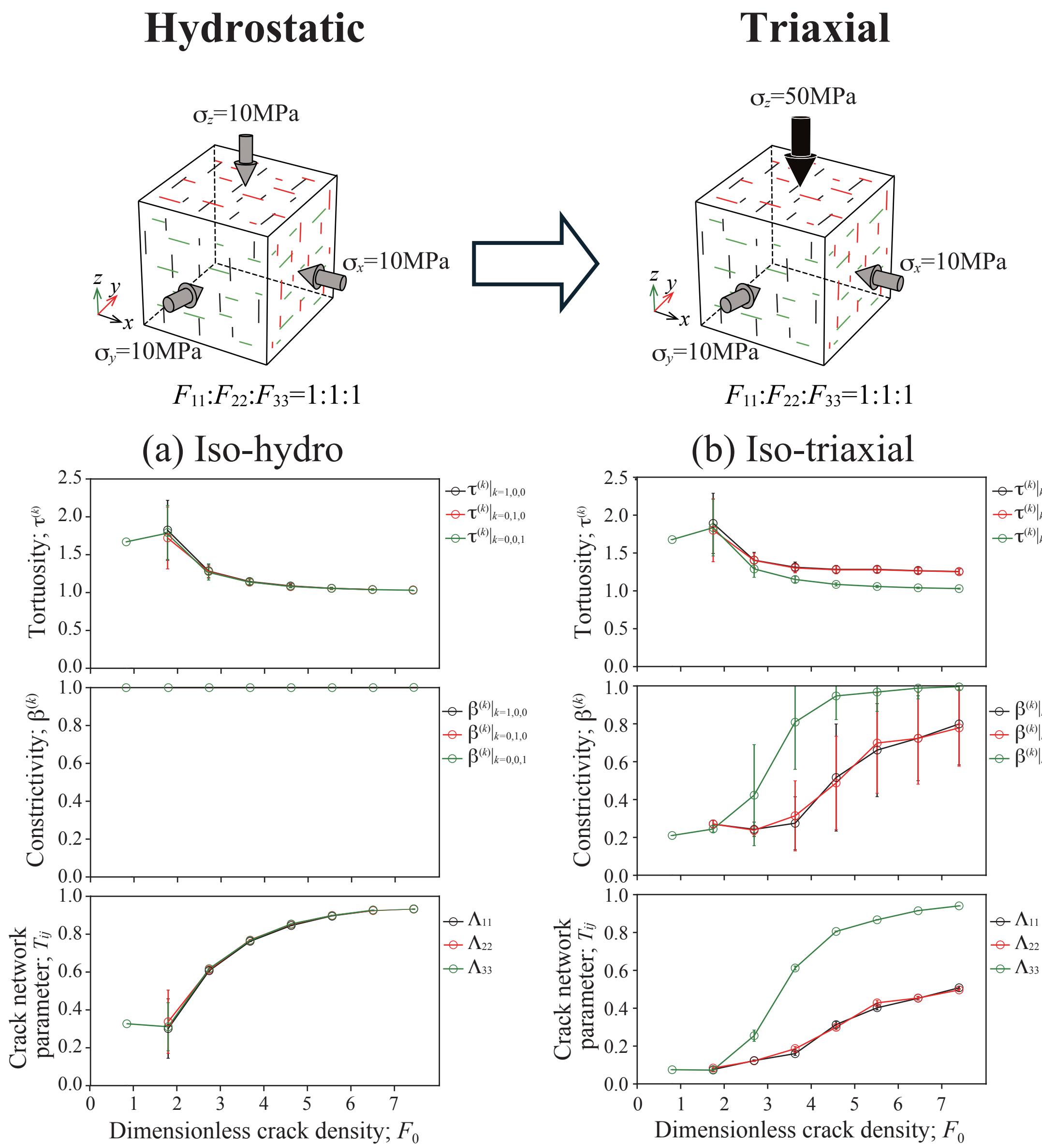

Fig. 10

Fig. 10 Examples of the variations in $\tau^{(k)}$, $\beta^{(k)}$, and T_{ij} with crack density under hydrostatic and triaxial conditions in the isotropic case.

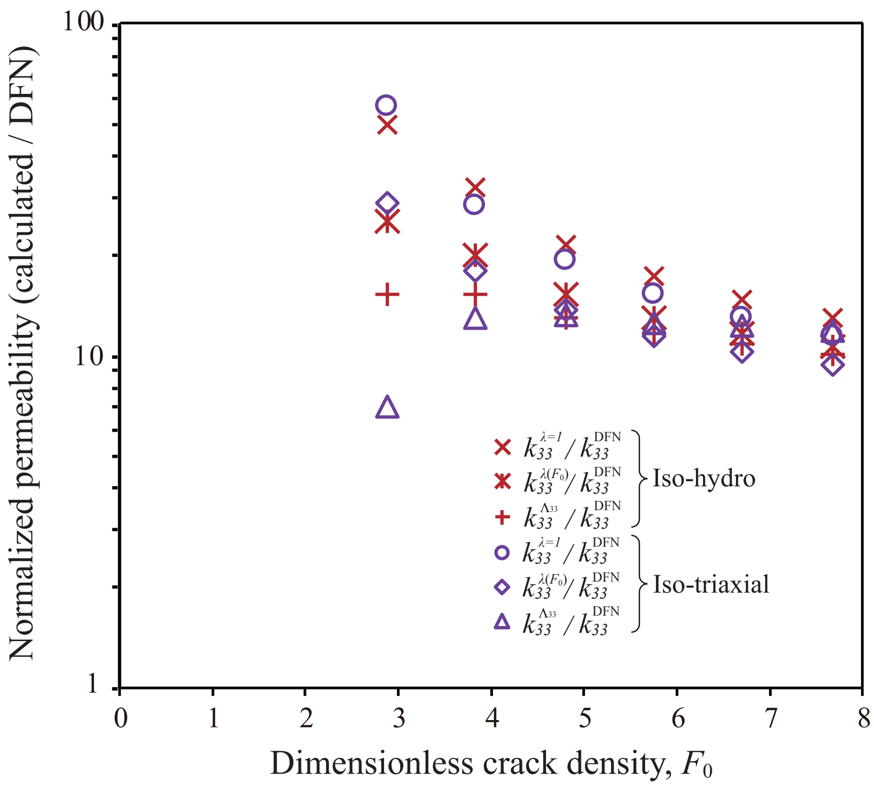

Fig. 11

Fig. 11 Variation of $k_{33}^{(\Lambda_{33})}$, $k_{33}^{(\lambda(F_0))}$, and $k_{33}^{(\lambda=1)}$, normalized by k_{33}^{DFN}, as a function of dimensionless crack density.

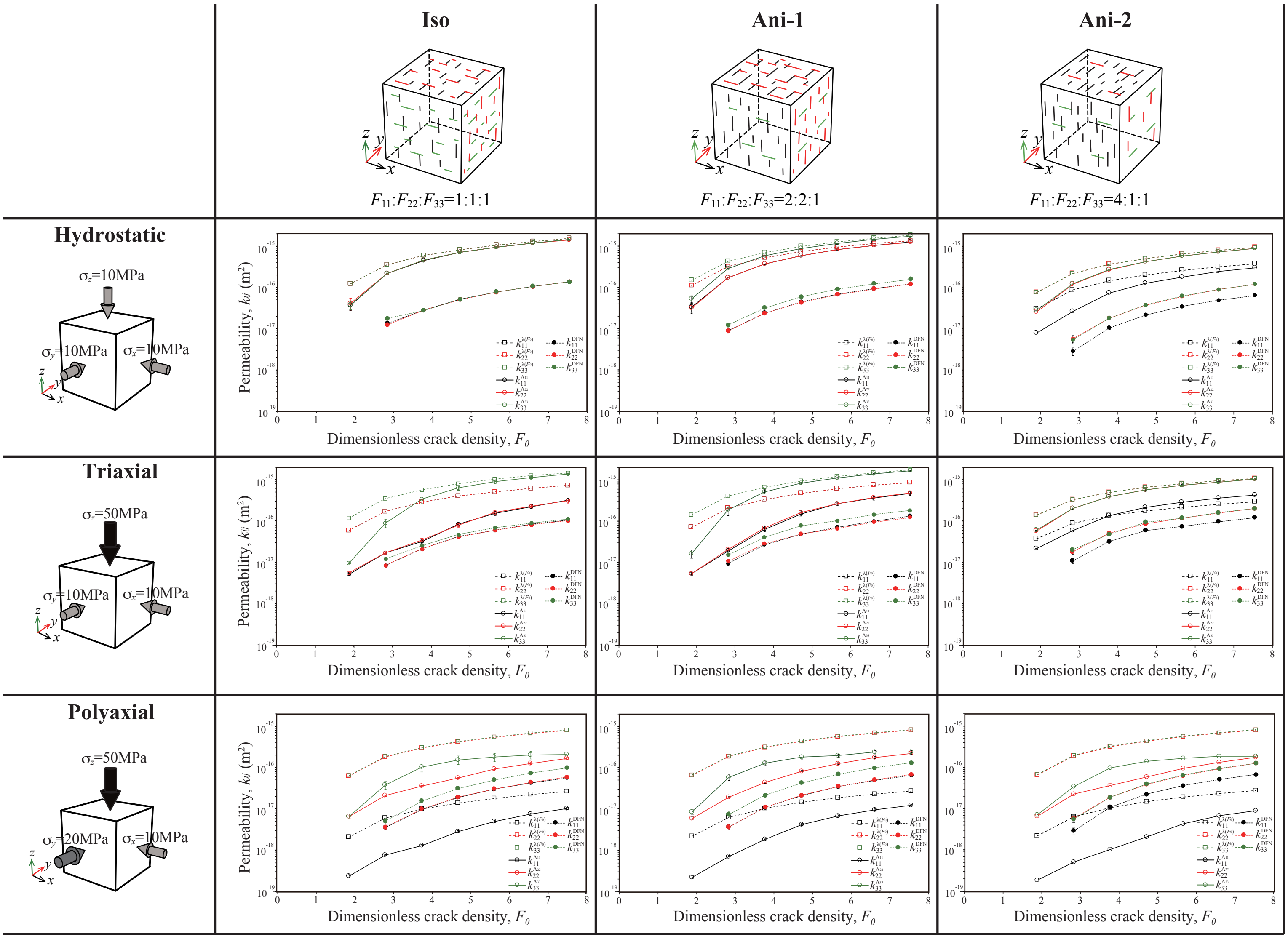

Fig. 12

Fig. 12 Changes in $k_{ij}^{(\Lambda_{ij})}$(solid lines), $k_{ij}^{(\lambda(F_0)}$(broken lines), and k_{ij}^{DFN}(dotted lines) as a function of dimensionless crack density for different stress and crack fabric conditions.

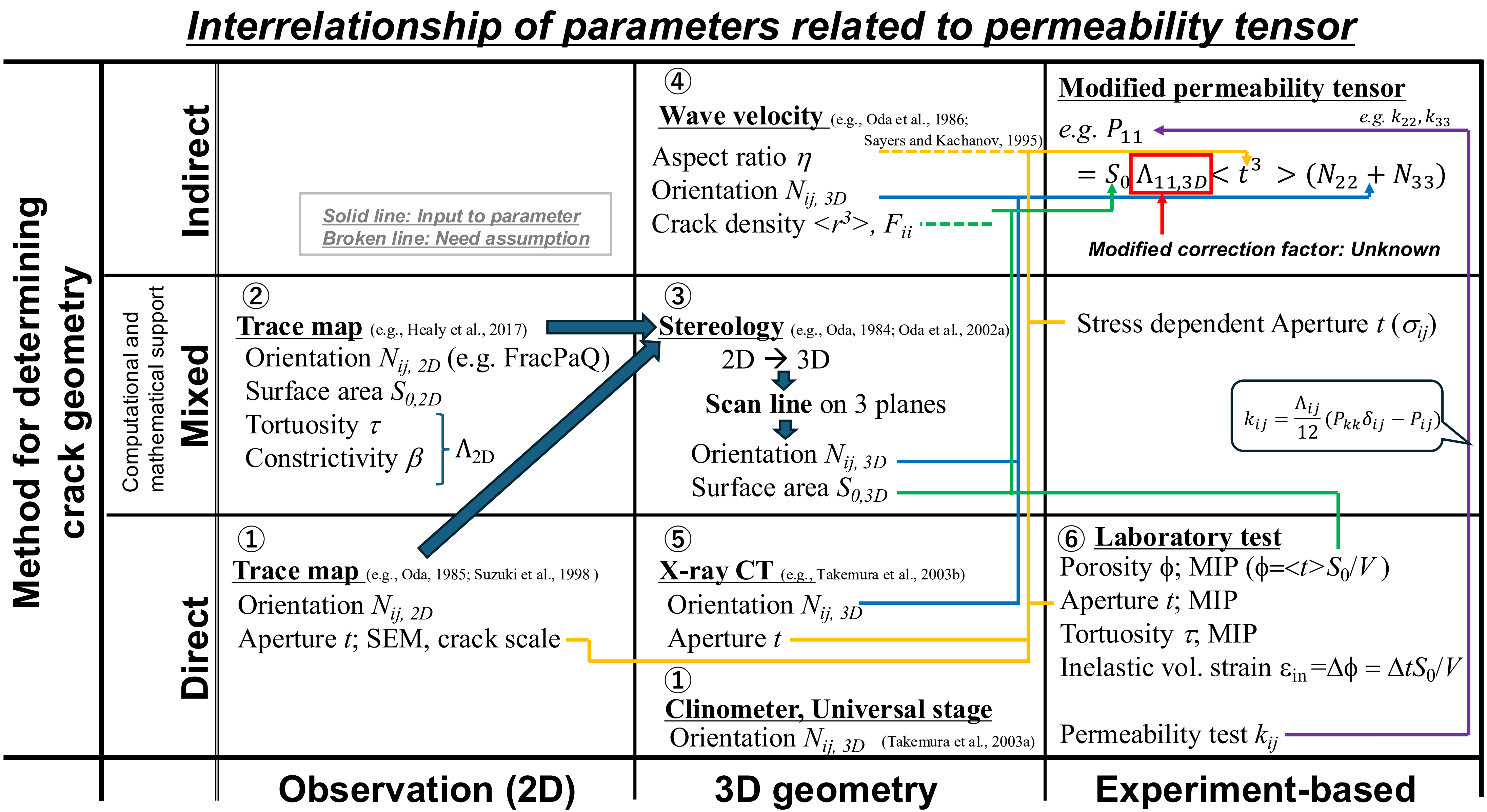

Fig. 13

Fig.13 Diagram illustrating the procedures for determining parameters associated with the permeability tensor.